ORIGINAL ARTICLE

Luminescent gold nanocluster-based sensing platform for accurate H₂S detection *in vitro* and *in vivo* with improved anti-interference

Qi Yu[1], Pengli Gao[1], Kenneth Yin Zhang[1], Xiao Tong[1], Huiran Yang[1], Shujuan Liu[1], Jing Du[1], Qiang Zhao[1] and Wei Huang[1,2]

Gold nanoclusters (Au NCs) are promising luminescent nanomaterials due to their outstanding optical properties. However, their relatively low quantum yields and environment-dependent photoluminescence properties have limited their biological applications. To address these problems, we developed a novel strategy to prepare chitosan oligosaccharide lactate (Chi)-functionalized Au NCs (Au NCs@Chi), which exhibited emission with enhanced quantum yield and elongated emission lifetime as compared to the Au NCs, as well as exhibited environment-independent photoluminescence properties. In addition, utilizing the free amino groups of Chi onto Au NCs@Chi, we designed a FRET-based sensing platform for the detection of hydrogen sulfide (H₂S). The Au NCs and the specific H₂S-sensitive merocyanine compound were respectively employed as an energy donor and acceptor in the platform. The addition of H₂S induced changes in the emission profile and luminescence lifetime of the platform with high sensitivity and selectivity. Utilization of the platform was demonstrated to detect exogenous and endogenous H₂S *in vitro* and *in vivo* through wavelength-ratiometric and time-resolved luminescence imaging (TLI). Compared to previously reported luminescent molecules, the platform was less affected by experimental conditions and showed minimized autofluorescence interference and improved accuracy of detection.

Light: Science & Applications (2017) **6**, e17107; doi:10.1038/lsa.2017.107; published online 1 December 2017

Keywords: bioimaging; gold nanoclusters; hydrogen sulfide; luminescent sensors; photoluminescence

INTRODUCTION

Photofunctional nanomaterials have been widely applied to the biomedical field owing to outstanding optical, chemical, and electrical properties[1–6] and have emerged as viable alternatives to small molecular probes. Current photofunctional nanomaterials used for biomedical applications include quantum dots, upconversion nanoparticles and gold nanoparticles, and each has merits and limitations. For instance, quantum dots have bright and size-tunable emission but are toxic and experience blinking[7–11]. Upconversion nanoparticles (UCNPs) are excitable by near-infrared light and allow imaging in deep tissues, but the upconversion efficiencies need to be improved[12–16]. Gold nanoparticles possess easy functionalization and color tunability, but are usually used as fluorescence quenchers because of their broad absorption spectrum and large molar absorption coefficients[17–21].

Gold nanoclusters (Au NCs) are a new type of luminescent nanomaterial[22–27]. Their small dimensions lead to molecule-like properties that are different from gold nanoparticles[24,25]. Au NCs display many interesting characteristics, such as good water solubility, high photostability, size-tunable emission maxima, large Stokes shifts,

good biocompatibility and easy bioconjugation. In addition, Au NCs capped with thiolate ligands display long emission lifetimes, which vary from hundreds of nanoseconds to microseconds[26,28]. The long lifetime enables to minimize the autofluorescence interference in biological samples through time-resolved luminescence techniques[29–32]. The downsides of Au NCs are their relatively low quantum yields and the environment-dependent photoluminescence. To address these problems, efforts have been made to improve the quantum yields and modify the surfaces of Au NCs to resist effects from their environment.

Herein, we developed a novel strategy using Chi-functionalized Au NCs (Au NCs@Chi) to enhance the quantum yields and improve the resistance to their environment. Au NCs@Chi were readily functionalized via the free amino groups of Chi to develop biological probes. As an example, we designed a novel sensing platform utilizing Förster resonance energy transfer (FRET) for the rapid detection of hydrogen sulfide (H₂S). H₂S were used for sensing because it is associated with the regulation of many biological processes, including vasodilation[33,34], anti-inflammation[35,36] and neurotransmission[37]. We employed the Au NCs as energy donors and the specific H₂S-sensitive merocyanine
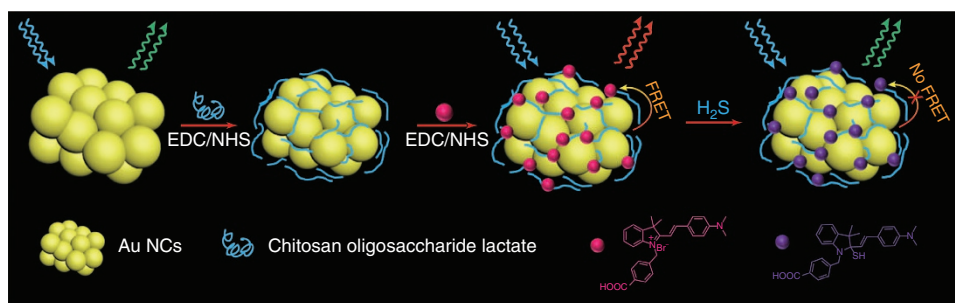
Figure 1 Schematic diagram of the nanoprobe.

derivative (Cy1) as an energy acceptor to construct a FRET platform (Figure 1). The sensing platform displayed dual emission bands and the band that was ascribed to Cy1 was dominated. Upon addition of H_2S, Cy1 responded dynamically to H_2S by decreasing the absorbance peak, inducing the blocking of the FRET process, and thus, the luminescence profile was dominated by the emission from the Au NCs. Both luminescence intensities were recorded and their ratio changes were calculated for wavelength-ratiometric detection. This ratiometric measurement avoided most ambiguities from the experiment conditions, such as the probe concentration and excitation laser power[38–40]. In addition, the efficient FRET process from the Au NCs to Cy1 gave rise to a long luminescence lifetime of the nanoprobe, which enabled the minimization of the autofluorescence interference in biological environments through TLI. Due to a significant change in emission lifetime upon interaction with H_2S, lifetime-based detection was possible. Similar to the ratiometric measurement, the influences from the probe concentration and the excitation pulsed power were reduced[41,42]. Hence, the dual-emissive nanoprobe was used for exogenous and endogenous H_2S detection in live HeLa cells and zebrafishes. The nanoprobe was demonstrated to maintain high H_2S sensitivity and display good resistance to interference from the external environment.

MATERIALS AND METHODS

The chemicals, reagents and characterization measurements are used according to the previous work[39,43] reported by our group. Cellular experiments used HeLa cells as examples, and were conducted according to the work[39]. The incubation concentration of Au NCs-Cy1 was 25 µg ml^{-1}. The cytotoxicity experiments were performed via the methyl thiazolyl tetrazolium (MTT) assay. Au NCs-Cy1 at different concentrations (12.5–200.0 µg ml^{-1}) were added to incubate cells in 96-well assay plate[44].

Au NCs were obtained by reduction using HAuCl$_4$, tetrakis(hydroxymethyl)phosphonium chloride (THPC) and 11-mercaptoundecanoic acid (MUA) under a basic environment. Chitosan oligosaccharide lactate (Chi) and chitosan were coated onto Au NCs through EDC/NHS chemistry. To investigate the effect of the concentration of Chi, various concentrations of Chi (0.5–5.0 mg ml^{-1}) were used for the preparation. In addition, we used the same method to obtain Au NCs@Chitosan with a varied molecular weight. The average molecular weights of chitosan used were 50–190, 190–310 and 310–375 kDa, respectively. Various concentrations of Cy1 (2, 20 and 200 µM) were used to investigate the effect of the concentration of Cy1 for the synthesis of Au NCs-Cy1. The detailed preparation processes are explained in the Supplementary Information.

RESULTS AND DISCUSSION

11-Mercaptoundecanoic acid (MUA)-functionalized Au NCs were obtained according to a one-pot strategy[45] through reducing process using a gold salt, THPC and MUA. Subsequently, Chi was assembled onto the Au NCs via reaction between the amino moieties of Chi and the carboxylic acid groups of the Au NCs to obtain Au NCs@Chi. The prepared MUA-capped Au NCs were characterized by transmission electron microscopy (TEM; Figure 2a). The average particle diameter was approximately 2 nm. HRTEM showed a lattice distance of 2.35 Å, which corresponds to the (111) lattice spacing of fcc gold. The elemental analysis of the Au NCs given by energy-dispersive X-ray spectroscopy (EDS; Supplementary Fig. S1) indicated that the sample was composed of gold (Au), sulfur (S), carbon (C) and oxygen (O). TEM confirmed that there was no aggregation of Au NCs after reaction with Chi (Figure 2b). It is hard to observe Chi through TEM because of the low contrast of Chi. The data obtained from dynamic light scattering showed that the hydrodynamic diameters of the Au NCs and Au NCs@Chi were 3.70 ± 0.64 and 9.66 ± 1.13 nm (Figure 2d and 2e), respectively, which demonstrated the successful coating of Chi.

The modification of the Au NCs with Chi was confirmed by zeta potential analysis and Fourier transform-infrared (FT-IR) spectroscopy. The FT-IR spectra (Figure 2g) of the MUA-capped Au NCs did not show any free S−H peak, indicating the ligation of the S atoms of MUA with the clusters. A band at ~2920 and 1730 cm^{-1} were assigned to −CH$_2$− stretching and C=O stretching modes of the carboxylic acid groups, respectively. After assembly of Chi onto the Au NCs, O−H bending (3310 cm^{-1}) and C−O stretching (1034 cm^{-1}) vibrations were found. A band appeared at 1531 cm^{-1}, which was attributed to the C=O from amide groups, indicating the covalent conjugation of Chi with the Au NCs. In addition, the conjugation of positively charged Chi led to an increase of the zeta potential from −45.9 to 32.3 mV (Figure 2h).

The Au NCs and Au NCs@Chi were characterized by UV/Vis absorption (Figure 3a). No characteristic broad surface plasmon resonance band (at ~520 nm) was observed, implying the absence of gold nanoparticles formed in solution. The obvious peak at 370 nm was ascribed to the molecular behavior of the Au NCs. No obvious difference was observed after assembly of Chi on the surface of the Au NCs. Upon photoexcitation, the MUA-capped Au NCs displayed a structureless emission band at 535 nm (Figure 3b), and the luminescence quantum yield in aqueous solution was measured to be 3.0%. The luminescence decay of the Au NCs in water was measured with excitation at 375 nm (Figure 3c). The biexponential decay curve displayed emission lifetimes of 47.9 ns (35.4%) and 349 ns (64.6%). The short component (47.9 ns) was ascribed to emission from singlet excited states[31,46,47], while the long component (349 ns) was attributed to charge transfer from the S atoms to the metal center. Further
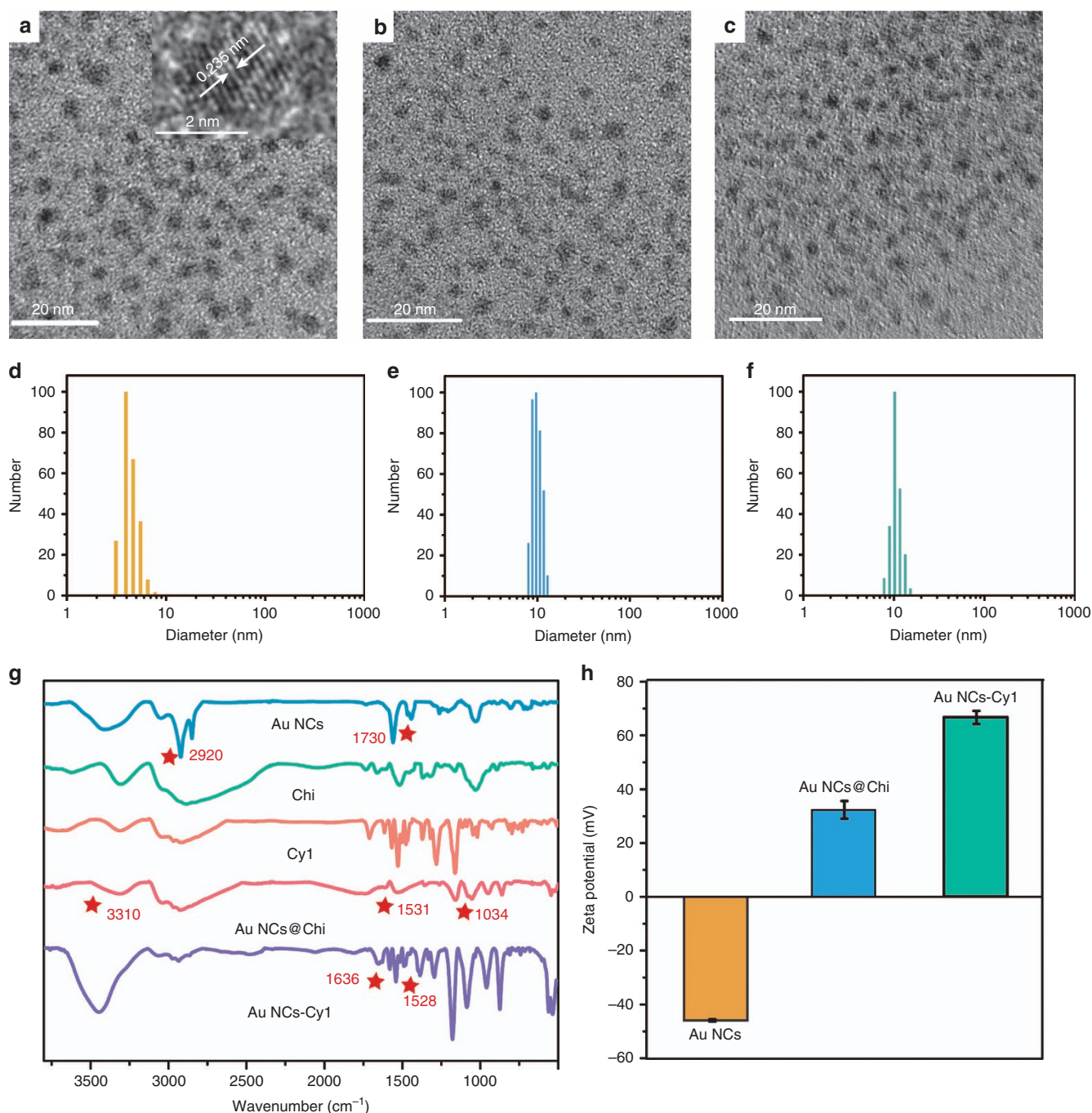
Figure 2 TEM images (**a–c**) and DLS results (**d–f**) of the Au NCs, Au NCs@Chi and Au NCs-Cy1; FT-IR spectra (**g**) of the Au NCs, Chi, Cy1, Au NCs@Chi and Au NCs-Cy1; zeta potentials (**h**) of the as-prepared Au NCs, Au NCs@Chi and Au NCs-Cy1 in water.

assembly of Chi did not affect the emission maximum of the Au NCs (Figure 3b), whereas the functionalization of Chi led to a quantum yield of 7.0%, which is higher than those of MUA-capped Au NCs previously reported[45,48–51]. Au NCs@Chi also displayed emission with a biexponential luminescence decay. The lifetimes of the two components were determined to be 188 ns (29.7%) and 710 ns (70.3%). Furthermore, we prepared Au NCs@Chi samples with varied concentrations of Chi ($0.5 - 5.0$ mg ml^{-1}). An increased concentration of Chi resulted in an enhanced quantum yield of Au NCs@Chi (see Supplementary Table S1 for details). The elongated emission lifetime and increased quantum yield of Au NCs@Chi may

be associated with decreased non-radiative processes due to the protection of Chi[52].

To demonstrate the effectiveness of the protection of Chi, we investigated the photoluminescence of the Au NCs and Au NCs@Chi when there were environmentally relevant metal ions in solution (Figure 3d). The emission of the Au NCs was quenched by 1 mM Ni^{2+}, Fe^{3+}, Cd^{2+}, Co^{2+} and Pb^{2+}, while that of Au NCs@Chi showed resistance to these ions. The quenching behavior may be attributed to the interaction between MUA and the metal ions. The interaction was weakened after the assembly of Chi. In addition, the stabilities of the photoluminescence of the Au NCs and Au NCs@Chi were studied in
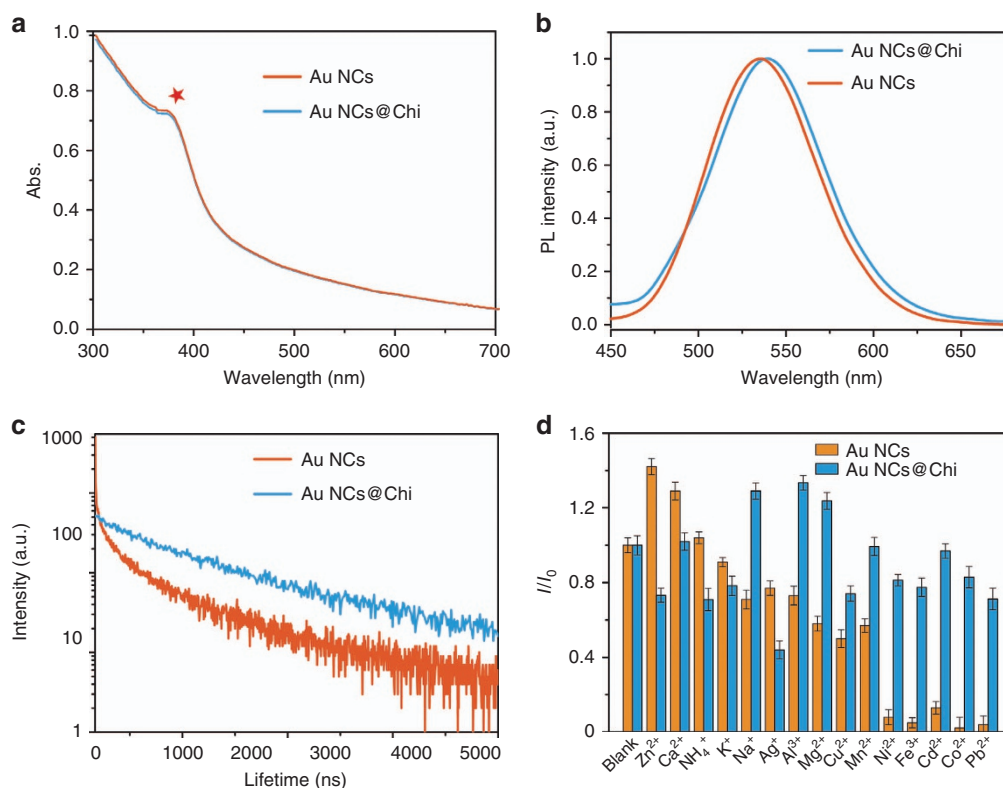
Figure 3 Absorption spectra (**a**), photoluminescence spectra (**b**) and photoluminescence decays (**c**) of the Au NCs and Au NCs@Chi in water. (**d**) Relative luminescence (I/I_0) at $\lambda_{ex} = 405$ nm of the Au NCs and Au NCs@Chi (25 μg ml^{-1}) with 1 mM of various metal ions being added.

different physiological environments, including in the presence of various anions, at different pH values (in the physiological range) and in the presence of biological molecules (Supplementary Fig. S2). The photoluminescence spectra of Au NCs@Chi showed small fluctuations, implying their good stability. The results demonstrated the possibility for the use of Au NCs@Chi as luminescent platforms in biological systems.

Encouraged by the good properties of Au NCs@Chi, we further used them to construct a sensing platform (Au NCs-Cy1) for the detection of H$_2$S. In the sensing system, as the Au NCs are unreactive toward H$_2$S (Supplementary Fig. S3), the Au NCs served as a reference material. Compound Cy1 was designed and synthesized as a responsive compound, since Cy1 shows absorption and luminescence responses toward H$_2$S due to specific nucleophilic addition[43]. More importantly, its absorbance overlaps well in wavelength with the emission band of the Au NCs (Supplementary Fig. S4), facilitating FRET from the nanoclusters to Cy1.

Au NCs-Cy1 was obtained by reacting Cy1 with Au NCs@Chi through amidation. The successful attachment of Cy1 onto Au NCs@Chi was demonstrated by FT-IR spectroscopy and zeta potential analysis. Compared with the FT-IR spectrum of Au NCs@Chi, new peaks at 1528 and 1636 cm^{-1} were illustrated in the spectrum of Au NCs-Cy1, which originated from the benzene stretching modes of Cy1 and the C=O stretching modes of the amide groups, respectively (Figure 2g). The zeta potential of Au NCs-Cy1 increased from 32.3 to 66.7 mV, implying the presence of the positively charged Cy1 compound (Figure 2h). In addition, the Au NCs after reaction with Cy1 were characterized by TEM and DLS (Figure 2c and 2f). No aggregation of Au NCs-Cy1 was observed in the TEM image, and the

DLS results displayed that the hydrodynamic diameter was 10.22 ± 1.98 nm. The absorption band of Au NCs-Cy1 at 568 nm (Supplementary Fig. S5) was attributed to Cy1. The mass ratio of Cy1 to Au was estimated to be ~0.097, which was obtained from the results of the absorption spectrum and inductively-coupled plasma atomic emission spectrometry. Furthermore, we studied the photoluminescence spectrum of Au NCs-Cy1. Upon excitation at 405 nm, dual emission bands respectively localized at 512 and 604 nm were present. These luminescence bands were assigned to the emission of the Au NCs and Cy1, respectively. Owing to the weak absorption of Cy1 at 405 nm, the emission band at 604 nm was ascribed to a FRET process. The average emission lifetime of the Au NCs was shortened in the nanoprobe compared to that in solution and simultaneously that the average emission lifetime of Cy1 was extended to 24.2 ns in the nanoprobe, which demonstrated the occurrence of FRET process. The Förster radius was estimated to be 1.92 nm, which was in accordance with the basic principles of a FRET process[53]. The luminescence photostability experiment of the nanoprobe showed that the emission bands centered at 512 and 604 nm maintained more than 88% and 85%, respectively, of their original luminescence after UV irradiation for 15 min (Supplementary Fig. S6), which is very much alike the good photostability of the Au NCs and Au NCs@Chi (Supplementary Fig. S7). In addition, the photoluminescence spectrum of the nanoprobe did not show any remarkable changes when the solution was left to stand for more than 3 months, indicating the high stability of the probe. The luminescence ratio was also independent of different ions (Supplementary Fig. S8).

The sensing behavior of the prepared Au NCs-Cy1 to NaHS (a commercially available H$_2$S donor) was investigated in PBS buffer
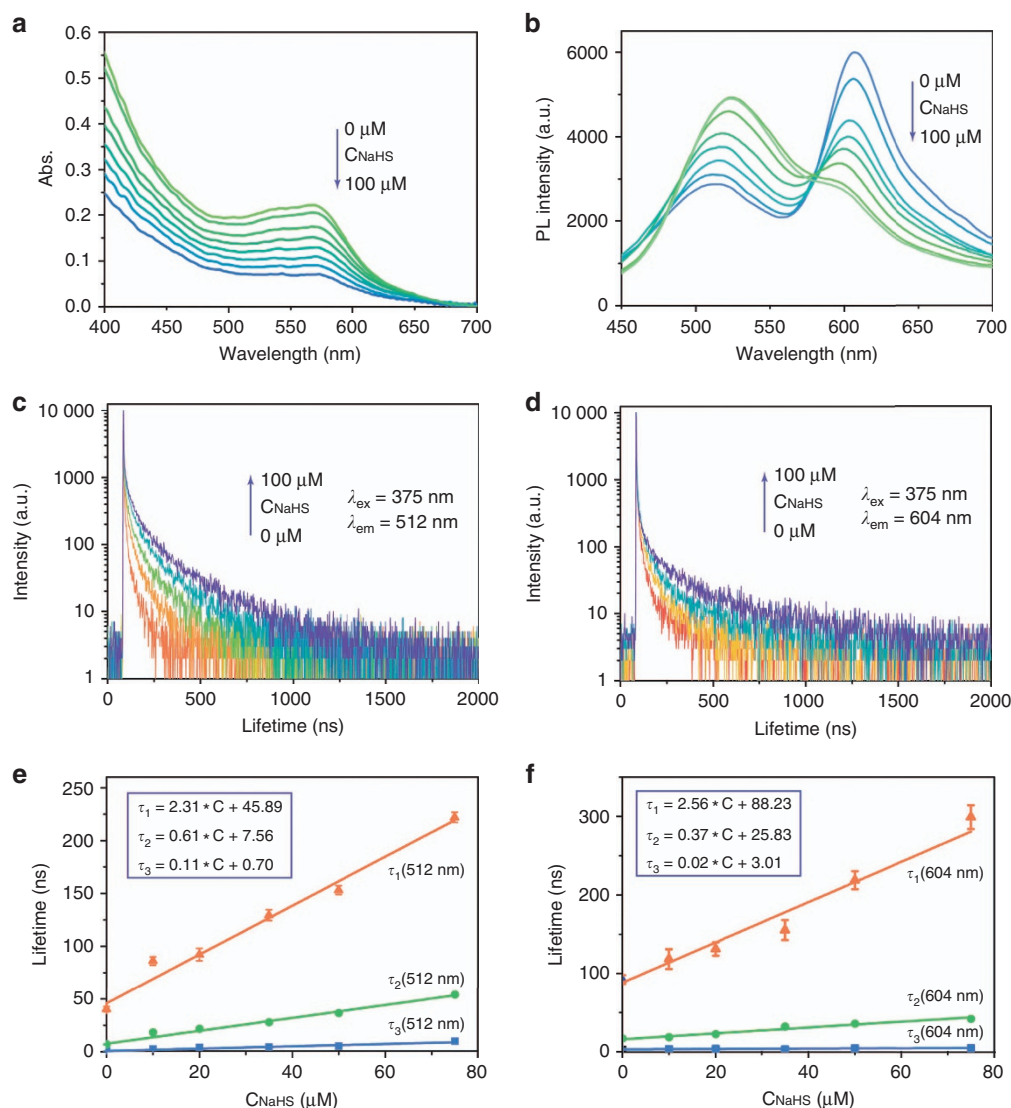
Figure 4 Absorption (**a**) and photoluminescence (**b**) spectra of Au NCs-Cy1 (25 µg ml^{-1}) in PBS (pH 7.4) with the addition of 100 µM NaHS. Changes in the time-resolved photoluminescence decay at 512 nm (**c**) and 604 nm (**d**) of Au NCs-Cy1 (25 µg ml^{-1}) upon addition of NaHS (0 – 100 µM) obtained with 375 nm excitation. (**e**) NaHS dependence of the lifetimes of the three exponentials required to fit the luminescence decay curves at 512 nm and the corresponding linear regressions. (**f**) NaHS dependence of the lifetimes of the three exponentials required to fit the luminescence decay curves at 604 nm and the corresponding linear regressions.

(Figure 4a and 4b), due to the good water solubility. The nanoprobe exhibited an obvious decrease of the absorption band at 568 nm when HS$^-$ concentration was enhanced from 0 to 100 µM (Figure 4a). The detailed photoluminescence titration was performed upon excitation at 405 nm (Figure 4b). Addition of 100 µM HS$^-$ led to distinct quenching of the emission band at 604 nm, while the band at 512 nm simultaneously exhibited a noticeable increment. The intensity ratio of the peaks at 512–604 nm was changed from 0.49 to 1.73 when HS$^-$ (0 – 100 µM) was added (Supplementary Fig. S9). The detection limit was calculated to be 1.83 µM, which represents a sufficient sensitivity for the detection of physiological H$_2$S levels[54].

To investigate the importance of the Chi concentration and low molecular weight for the sensing system, we first used different concentrations of Chi (0.5 – 5.0 mg ml^{-1}) for the preparation of Au NCs@Chi. DLS experiments of Au NCs@Chi that were freshly prepared and stored after 15 days (Supplementary Fig. S10) were conducted. The diameters of Au NCs@Chi showed no significant

changes, demonstrating that they were well dispersed in water. TEM images of the obtained nanoparticles were consistent with the results obtained from DLS (Supplementary Fig. S11a–S11c). The emission maximum showed no shift when the Chi concentration was increased (Supplementary Fig. S12). Furthermore, they were modified with Cy1 and dispersed in PBS buffer for H$_2$S detection. When the concentration of Chi was increased, the luminescence intensity ratios of Au NCs-Cy1 were similar with only small fluctuations (Supplementary Fig. S13), and the detection limits of these probes were determined to be 1.91, 1.82 and 2.06 µM. The similar sensitivity of the probes was ascribed to the sufficient number of Cy1 molecules attached on Chi. To balance the small size and good PL properties of the nanoprobe, we selected 1.0 mg ml^{-1} Chi for Au NCs@Chi in further experiments.

In addition, Au NCs with varied average molecular weights of chitosan were prepared. The high viscosity of chitosan resulted in an increased hydrodynamic diameter, and the diameter slightly increased over 15 days (Supplementary Fig. S14). TEM images of the obtained
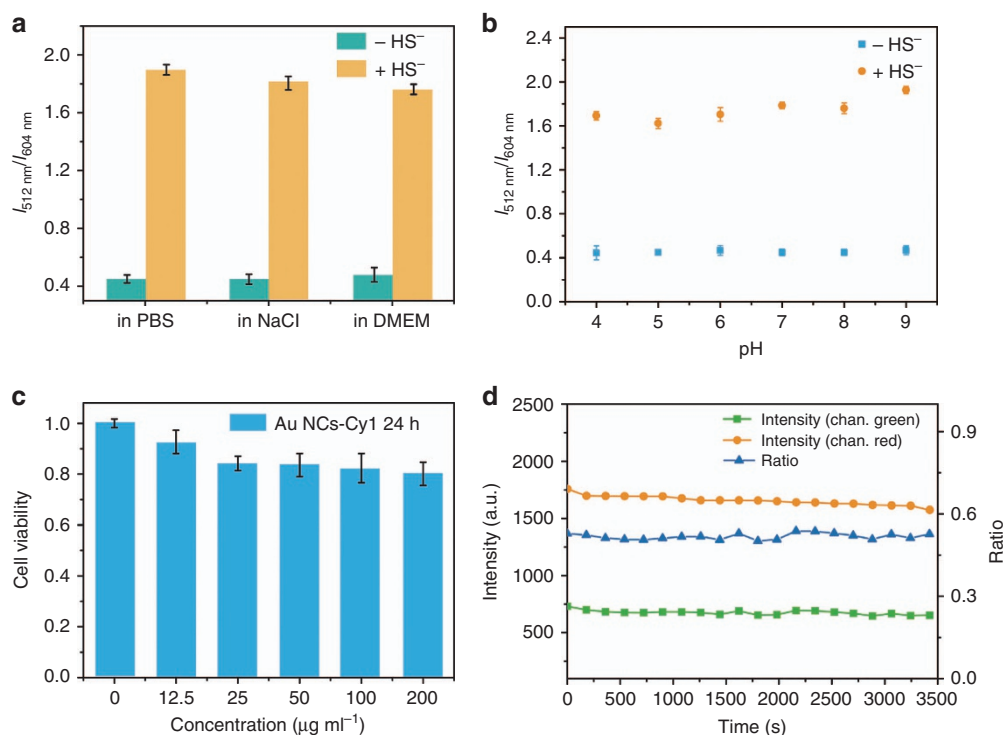
Figure 5 (**a**) The emission ratios (I_{512}/I_{604}) of Au NCs-Cy1 (25 µg ml^{-1}) in PBS buffer, in NaCl solution (50 mM) and in a cell culture, DMEM, before and after 100 µM NaHS was added; (**b**) stability of the emission ratio (I_{512}/I_{604}) of Au NCs-Cy1 (25 µg ml^{-1}) at different pH values; (**c**) cytotoxicity of Au NCs-Cy1 on living HeLa cells analyzed via the MTT experiment; (**d**) photostability of Au NCs-Cy1 (25 µg ml^{-1}) in live cells. Emission wavelengths: 520 ± 10 nm and 610 ± 20 nm; excitation wavelength: 405 nm.

nanoparticles were consistent with the results obtained from DLS (Supplementary Fig. S11d and S11e). The emission maximum showed no shift when the average molecular weight of chitosan was increased (Supplementary Fig. S15). Au NCs@chitosan with different average molecular weights (190–310 kDa and 310–375 kDa) showed low quantum yields compared to those with low average molecular weight (50–190 kDa; see Supplementary Table S2 for details). The decreased quantum yield of Au NCs@chitosan and the increased donor⁻ acceptor distance may lead to a low FRET efficiency of Au NCs-Cy1, thus inducing poor response to H₂S (Supplementary Fig. S16). These results showed that chitosan oligosaccharide lactate with a low molecular weight is advantageous for the preparation of the nanoprobe with a small diameter and makes it possible to improve the sensitivity of the nanoprobe.

More experiments were carried out to determine the relation between the FRET efficiency and sensitivity of the nanoprobe with various concentrations of Cy1. We used different concentrations of Cy1 to modify Au NCs@Chi. The FRET efficiencies of these prepared probes were 22.3%, 60.9% and 88.1%, and the response of the luminescence ratio to H₂S is illustrated in Supplementary Fig. S17. The increased concentration of Cy1 resulted in a better response of the probe to H₂S. The detection limit was determined to be 12.4, 2.71 and 1.78 µM for the various concentrations. These results showed that the increased concentration of Cy1 improved the FRET efficiency and sensitivity of the probe.

Furthermore, the response rate of Au NCs-Cy1 toward HS⁻ was investigated. When 100 µM HS⁻ was added, the response was completed within 90 s (Supplementary Fig. S18a), which is faster than the response time of other reported probes for the detection of HS⁻ [55–57]. In addition, the rapid and sensitive response of Au NCs-Cy1 was

only remarkably triggered by HS⁻. Other competing analytes, such as halogen ions, reactive oxygen species and reactive nitrogen species, were also added to the system, and they showed little effect on the luminescence (Supplementary Fig. S18b). The ratiometric enhancement induced by HS⁻ was not interrupted when there were glutathione (GSH), homocysteine (Hcy) or cysteine (Cys) in the solution, thus reinforcing the good selectivity of the H₂S-mediated nucleophilic addition due to the relatively lower pK$_a$ value (~7.0) of H₂S than that of other biothiols[58]. These results show the high sensitivity and selectivity of Au NCs-Cy1 to H₂S.

In view of the long emission lifetime of Au NCs-Cy1, we investigated the luminescence lifetime sensing behavior for H₂S. Figure 4c presents the relation between luminescence lifetime changes of Au NCs-Cy1 and the HS⁻ concentration. The luminescence of Au NCs-Cy1 at 512 and 604 nm exhibited multi-exponential decays. A total of three exponential functions were required in the photoluminescence decay fitting of Au NCs-Cy1 (see Supplementary Tables S3–S4 for details). Prior to HS⁻ addition, the average emission lifetimes, τ_{ave}, at 512 and 604 nm were 25.6 and 24.2 ns, respectively, which demonstrated the presence of FRET process. The three components of the lifetime at 512 nm were linearly elongated with an increase of HS⁻ concentration (Figure 4e), due to the fact that FRET was inhibited by the reaction with HS⁻. Interestingly, the presence of HS⁻ also led to an elongation of the average lifetime at 604 nm (Figure 4d). The shortest lifetime component originated from Cy1 showed very small changes (Figure 4f), while its fractional weight was decreased as the result of the blocked FRET process (see Supplementary Table S4 for details). The longer components, which may be ascribed to the luminescence tail of the Au NCs, were elongated and dominant (Figure 4f). The lifetime changes upon
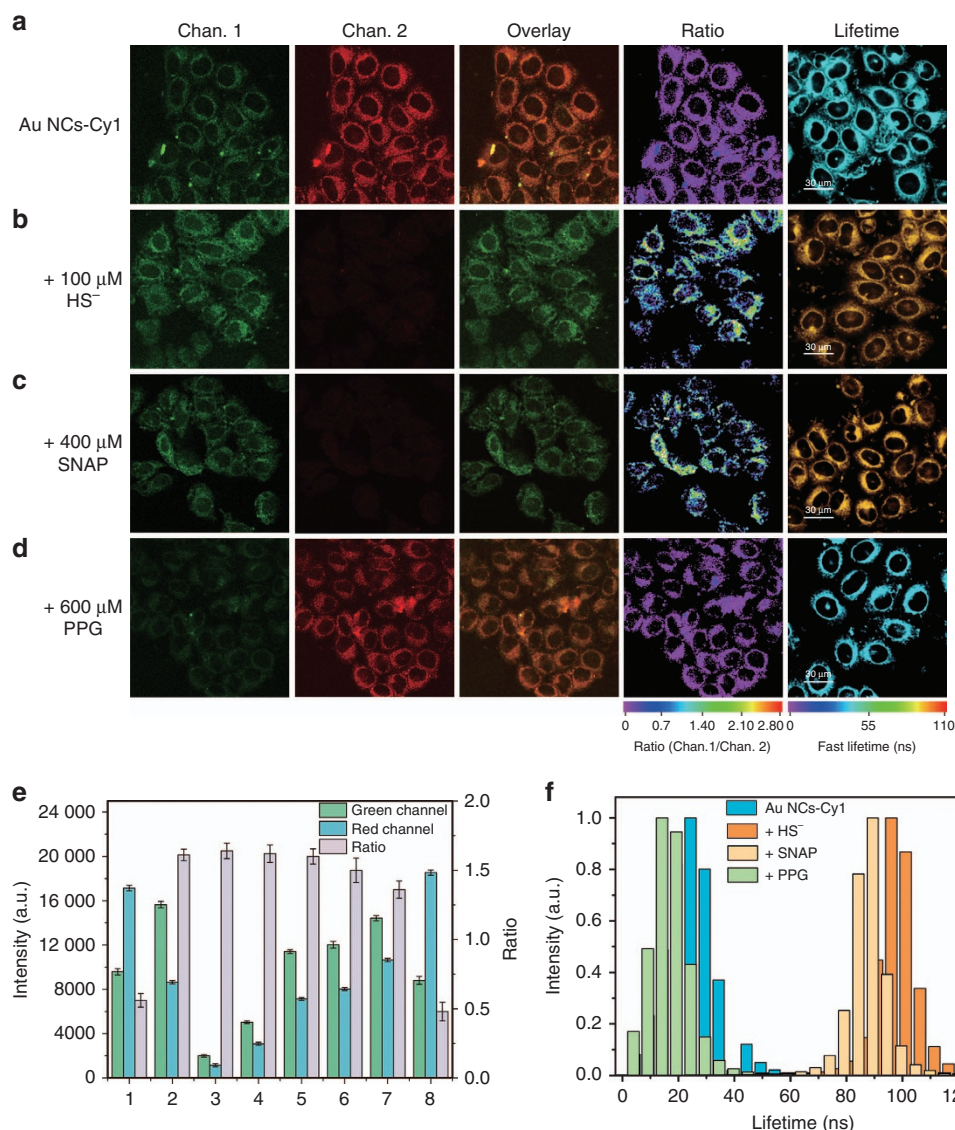
Figure 6 Confocal laser scanning microscopy, ratiometric and PLIM images of the HeLa cells treated with Au NCs-Cy1 (25 µg ml^{-1}) for 2 h at 37 °C (**a**), Au NCs-Cy1 loaded cells that was incubated with NaHS for 1 h (**b**), and the cells stimulated with SNAP (**c**) and PPG (**d**) and incubated with Au NCs-Cy1 for 2 h at 37 °C. (**e**) Intracellular luminescence intensities recorded from the green and red channels and the ratiometric signal of green to red channel (Ratio). The luminescence intensities and ratiometric signals were determined from the cells incubated with Au NCs-Cy1 (1), in the presence of NaHS (2), and stimulated with SNAP (7) and PPG (8). Control experimental conditions: (3) luminescence intensity of the cells incubated with Au NCs-Cy1 collected at 25 °C in the presence of NaHS. (4) HeLa cells with NaHS treated with Au NCs-Cy1 (10 µg ml^{-1}) for 2 h. (5) the time of incubation of cells with NaHS was elongated to 4 h; (6) the cells were illuminated under increased laser power in the presence of NaHS. These results were obtained by flow cytometry analysis; (**f**) average lifetime histograms of intracellular Au NCs-Cy1, followed by incubation with NaHS and stimulation with SNAP and PPG. Excitation wavelength was 405 nm; lifetimes were collected through a 520 ± 20 nm bypass filter.

H$_2$S concentration make Au NCs-Cy1 a suitable lifetime-based sensor for H$_2$S.

Considering the complex intracellular microenvironments, such as diverse salt, pH changes and protein concentrations, we checked the stability of the emission response of Au NCs-Cy1 under the following different conditions (Figure 5a and 5b): (1) over a broad pH range, (2) with the addition of excess salt, and (3) dispersed in a cell culture, DMEM. The results showed that the ratiometric luminescence response was independent of the pH value (4−9), NaCl solution (50 mM), and presence of the cell culture. In addition, we tested the effect of metal ions and proteins on the detection of H$_2$S (Supplementary Fig. S19). Except K$^+$ and Na$^+$, other metal ions with high concentrations showed intense effects on the response of the probe for the detection of H$_2$S due to the strong affinity between the metals and sulfide ions. However, the concentrations of these free metal ions are below 10^{-7} M in cells according to previous reports[59–63]. The luminescence ratio changes with these metal ions (10^{-7} M) being added demonstrated that these metal ions with low concentrations showed only small effects on the detection of H$_2$S. The sensing properties of the probe to H$_2$S were investigated in the presence of different proteins. Proteins, including BSA, pepsin, thrombin, lysozyme, trypsin and hemoglobin, were used. The presence of proteins

led to small fluctuations in the luminescence ratio changes when NaHS was added.

Biocompatibility is a key for success when applying Au NCs-Cy1 *in vitro*. The biocompatibility of Au NCs-Cy1 was determined by MTT assay (Figure 5c)[64]. The viability of cells treated with final concentrations of Au NCs-Cy1 (0, 12.5, 25, 50, 100 and 200 µg ml^{-1}) remained more than 80% after 24 h incubation, indicating that the as-prepared Au NCs-Cy1 showed the low cytotoxicity.

To explore systematically the uptake of Au NCs-Cy1 by living HeLa cells, a series of experiments were performed (Supplementary Fig. S20). First, Au NCs-Cy1 (25 µg ml^{-1}) added into the cell culture for 2 h incubation at 4 °C to ensure whether the uptake mechanism of Au NCs-Cy1 underwent a passive or active process. The cells incubated at 4 °C displayed weak luminescence (Supplementary Fig. S20b) compared to that at 37 °C (Supplementary Fig. S20a), which suggested that the uptake of Au NCs-Cy1 underwent an energy-relying process. Second, the effects of endocytotic and metabolic inhibitors on the cellular uptake of Au NCs-Cy1 were investigated (Supplementary Fig. S20c and S20d). After the cells were incubated with Au NCs-Cy1 and well-documented inhibitors (2-deoxy-D-glucose and olimycin, NH$_4$Cl), the luminescence intensities were significantly decreased. The cellular uptake of Au NCs-Cy1 was measured through flow cytometry (Supplementary Fig. S20e). The luminescence ratio of the green to red channels were consistent to that obtained from luminescence images, which indicates that Au NCs-Cy1 is stable in the cells, and entered the cells through an energy-dependent and endocytotic pathway.

Photobleaching is another problem that limits the application of the luminescent probes in biological samples. When the HeLa cells were incubated with 25 µg ml^{-1} Au NCs-Cy1, the luminescence intensities in the green and red luminescence channels were monitored for 1 h under the illumination of a 405 nm laser (Figure 5d). Although we observed slight variations in the luminescence intensities because of the fluctuation of the excitation pulsed power, the luminescence intensity ratio of green to red luminescence was almost unchanged. The above results demonstrated that Au NCs-Cy1 is a promising probe for biological applications.

The use of Au NCs-Cy1 to visualize intracellular H$_2$S was determined via laser scanning confocal microscopy. As illustrated in Figure 6a, the cells loaded with 25 µg ml^{-1} Au NCs-Cy1 for 2 h displayed dual luminescence in both channels, and the red luminescence was more intense than the green one. Further addition of HS$^-$ (100 µM) in the cell culture for 1 h significantly enhanced the green luminescence, while decreased the red one (Figure 6b). The corresponding luminescence ratio of the green to red channel changed from 0.51 to 1.56 in the presence of 100 µM NaHS (Figure 6b and 6e). The small discrepancy of response of Au NCs-Cy1 to H$_2$S between in buffer and in the cells may ascribe to the intracellular microenvironments that are more complicated than aqueous system. In addition, Au NCs-Cy1 was also used to ratiometrically monitor endogenously generated H$_2$S in the HeLa cells. *S*-Nitroso-*N*-acetyl-dl-penicillamine (SNAP) was used as an irritant to generate endogenous H$_2$S[65]. The SNAP (400 µM)-treated cells that were followed by incubation with Au NCs-Cy1 for 2 h displayed an increase of the luminescence ratio by
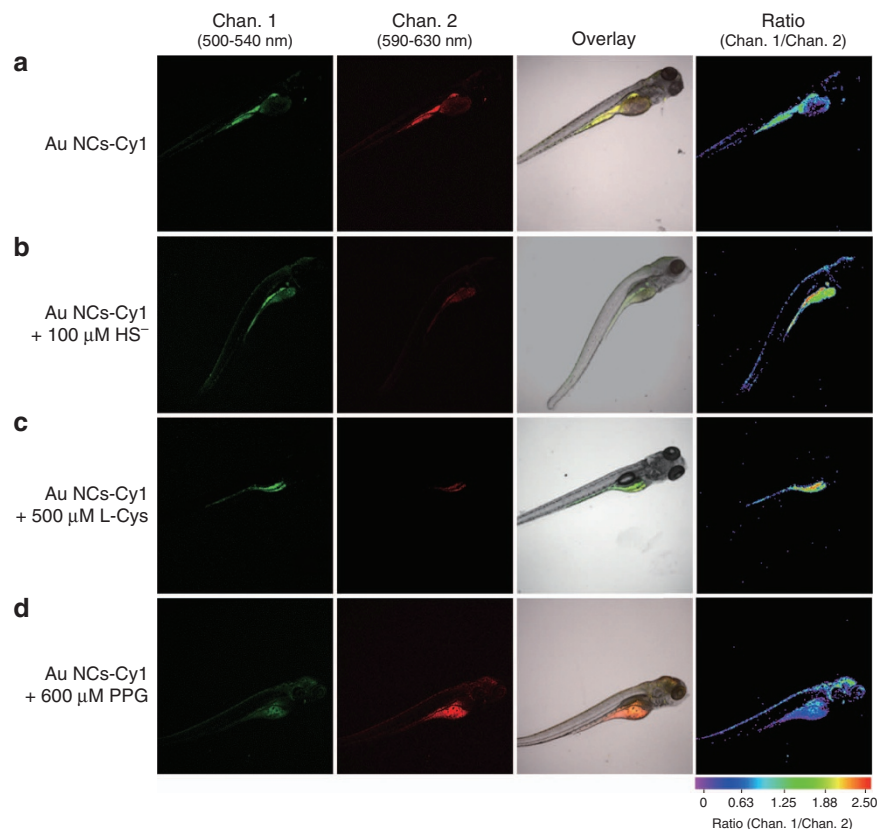

Figure 7 Confocal laser scanning microscopy and bright and ratiometric luminescence images of zebrafish after injection of Au NCs-Cy1 (25 µg ml^{-1}) at 37 °C (**a**), Au NCs-Cy1 loaded zebrafish that were treated with NaHS for 1 h (**b**); zebrafish stimulated with L-cysteine (**c**) and PPG (**d**) and injected with Au NCs-Cy1 (25 µg ml^{-1}) at 37 °C. The green channel was acquired by collecting the luminescence at 520 ± 20 nm (Chan. 1), while the red channel corresponded to 610 ± 20 nm (Chan. 2). The ratiometric luminescence images were the ratio of Chan 1. to Chan. 2.

a factor of 2.8 (Figure 6c and 6e). In addition, 600 μM DL-propargylglycine (PPG), an inhibitor of endogenous H_2S[66], was added to the cell culture for 30 min incubation to conduct a parallel experiment. Interestingly, the luminescence ratio of the PPG-treated cells was detected to be 0.48, which was lower than that of the Au NCs-Cy1-loaded cells (0.51) (Figure 6d–6e). The slight difference of the luminescence ratio in the cells may be attributed to a low dose of H_2S production in the cells. We utilized Photoluminescence lifetime imaging microscopy (PLIM) to detect exogenous and endogenous generation of H_2S in the cells (Figure 6a–6d). The HeLa cells treated with Au NCs-Cy1 (25 μg ml^{-1}) showed an average luminescence lifetime of approximately 24.3 ns (Figure 6a and 6f). The slight difference of the lifetime values between the cells and aqueous solution was attributed to the complex physiological environment. Similar to the variation trend in aqueous solution, further incubation with NaHS (100 μM) for 1 h elongated the lifetime to approximately 96.0 ns due to the blocked FRET process (Figure 6b and 6f). When the cells were stimulated with SNAP, Au NCs-Cy1 displayed a long lifetime of approximately 91.6 ns (Figure 6c and 6f), which demonstrated that endogenous HS$^-$ led to a lower response from Au NCs-Cy1 compared to exogenous HS$^-$. When the commonly used H_2S inhibitor, PPG, was added into the culture, the lifetime was determined to be approximately 14.1 ns (Figure 6d and 6f). All these obtained results indicated that Au NCs-Cy1 could be engaged as a sensitive sensor intracellular HS$^-$ via PLIM imaging.

To ensure whether the ratiometric and lifetime-based detection is resistant to external influences in intracellular detection, we designed the parallel experiments for the ratiometric H_2S imaging. In these experiments, the difference of experimental conditions included decreased incubation temperature, decreased incubation concentration of the nanoprobe, elongated incubation time and enhanced laser power for detection. Confocal luminescence imaging showed that, in contrast to the fluctuant luminescence intensity, the ratio was only associated with HS$^-$ (Supplementary Fig. S21a–S21d) and was independent of the nanoprobe concentration, incubation time, or excitation power. The data obtained from the flow cytometry analysis also supported this conclusion (Figure 6e, Supplementary Fig. S21e–S21i). Since the incubation temperature and time also affected the probe concentration in cells, we used these two conditions as well as decreasing the incubation concentration to investigate the resistance of the lifetime-based detection to probe concentration. Similarly, the lifetime values were only influenced by HS$^-$ (Supplementary Fig. S22) and were not affected by the excitation pulsed power and probe concentration.

Encouraged by the good results obtained in the intracellular environment, we also attempted to detect exogenous and endogenous generation of H_2S in live zebrafishes. The wild-type 5-day-old zebrafish were injected with 25 μg ml^{-1} Au NCs-Cy1. As illustrated in Figure 7a, the luminescence from the green and red channels varied in intensity, with an I_{green}/I_{red} ratio of 0.9. The ratio increased upon the addition of NaHS and L-cysteine, which is a substrate to generate

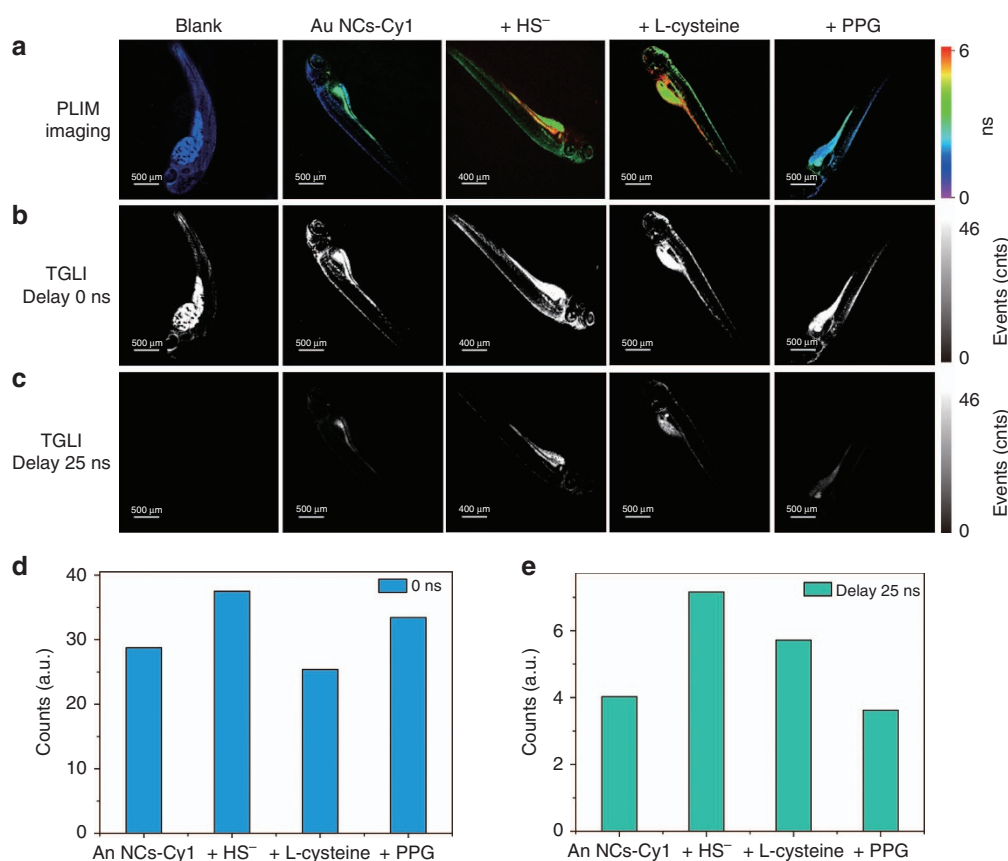**Figure 8** PLIM (**a**) and TGI (**b,c**) images of live zebrafish before and after injection of Au NCs-Cy1 (25 μg ml^{-1}), followed by treatment with NaHS (100 μM) for 1 h; zebrafish stimulated with L-cysteine (500 μM) and PPG (600 μM) and injected with Au NCs-Cy1 (25 μg ml^{-1}) at 37 °C; Lifetimes were collected through a 520 ± 20 nm bypass filter; luminescence intensity recorded from TGI images without (**d**) and with (**e**) a time delay.

H_2S (Figure 7b and 7c)[67]. The stimulation of PPG resulted in a decrease of the ratio (Figure 7d). Au NCs-Cy1 was demonstrated to show feasible H_2S sensing in zebrafishes.

We subsequently examined the capability of the lifetime-based H_2S sensing in zebrafish larva using PLIM. Unfortunately, the emission lifetime of Au NCs-Cy1 in zebrafish was shorter than that in the cells, which may arise from unavoidable interference of the intense autofluorescence. Although the emission lifetime of Au NCs-Cy1 was shortened in a real environment, Au NCs-Cy1 displayed a distinguishable lifetime compared to the autofluorescence in the zebrafish (Figure 8a). PLIM revealed that the lifetime of Au NCs-Cy1 detected through a bandpass filter (520 ± 20 nm) was average ~ 2.2 ns. Treatment with NaHS and L-cysteine increased the lifetime to 5.5 and 5.1 ns, respectively, while the addition of 600 μM PPG shortened the lifetime to 1.8 ns. These results showed the sensitivity of Au NCs-Cy1 to visualize endogenous H_2S. To further prove the existence of long-lived signals from Au NCs-Cy1, a time-gated imaging (TGI) measurement was conducted to investigate the Au NCs-Cy1-treated zebrafish (Figure 8b and 8c). Images that collected signal after exerting a time delay of 25 ns revealed that the intense autofluorescence in the zebrafish was not observed, while the images of the Au NCs-Cy1-treated zebrafish without delay time displayed intense signals, which indicated that the long-lived nanoprobe had advantages of anti-interference from the autofluorescence. Furthermore, the emission signals from Au NCs-Cy1 with different stimulation were monitored by TGI (Figure 8d and 8e). An interesting observation was that treatment with NaHS and L-cysteine enhanced the long-lived luminescence signal ($\tau > 25$ ns). Both changes were more obvious (Figure 8e) compared to that detected without a time delay (Figure 8d). A decreased intensity was also detected when PPG was added to inhibit the generation of H_2S (Figure 8e). These results showed that the TGI technique could eliminate autofluorescence and increase the signal-to-noise (S–N) ratio for the H_2S sensing.

CONCLUSIONS

In the article, we designed and obtained Au NCs@Chi, which exhibited emission with enhanced quantum yield, elongated emission lifetime and remarkable photophysical stability over Au NCs. The free amino groups onto the cluster permits Au NCs@Chi to be further modified and can serve as a potential nanoplatform for biological applications. Furthermore, we employed Au NCs@Chi to construct a sensing platform applied to detect exogenous and endogenous H_2S through ratiometric and time-resolved luminescence imaging. In contrast to an intensity-based measurement, both ratiometric and time-resolved methods can avoid interference from the probe concentration and excitation pulsed power and improve the accuracy of detection. In addition, the time-resolved luminescence imaging can minimize the interference of background fluorescence and increase the S–N ratio. The disadvantage of this probe was the small optical penetration depth, which inhibited its applications in mouse models. Hence, the further development of a near-infrared probe for H_2S sensing is currently under investigation. Moreover, the sensing platform developed in this work is not limited to H_2S and can be further applied to develop many ratiometric and long-lived luminescent sensors for specific analytes through the conjugation of different responsive organic compounds onto Au NCs@Chi. The utilization of the sensing platform will enable high accuracy and improve anti-interference in physiological detection.

CONFLICT OF INTEREST

The authors declare no conflict of interest.

1 Wolfbeis OS. An overview of nanoparticles commonly used in fluorescent bioimaging. *Chem Soc Rev* 2015; **44**: 4743–4768.
2 Konvalina G, Haick H. Sensors for breath testing: from nanomaterials to comprehensive disease detection. *Acc Chem Res* 2014; **47**: 66–76.
3 Li JJ, Cheng FF, Huang HP, Li LL, Zhu JJ. Nanomaterial-based activatable imaging probes: from design to biological applications. *Chem Soc Rev* 2015; **44**: 7855–7880.
4 Baptista FR, Belhout SA, Giordani S, Quinn SJ. Recent developments in carbon nanomaterial sensors. *Chem Soc Rev* 2015; **44**: 4433–4453.
5 Chinen AB, Guan CM, Ferrer JR, Barnaby SN, Merkel TJ *et al*. Nanoparticle probes for the detection of cancer biomarkers, cells, and tissues by fluorescence. *Chem Rev* 2015; **115**: 10530–10574.
6 Lim EK, Kim T, Paik S, Haam S, Huh YM *et al*. Nanomaterials for theranostics: recent advances and future challenges. *Chem Rev* 2015; **115**: 327–394.
7 Wegner KD, Hildebrandt N. Quantum dots: bright and versatile in vitro and in vivo fluorescence imaging biosensors. *Chem Soc Rev* 2015; **44**: 4792–4834.
8 Zhou J, Yang Y, Zhang CY. Toward biocompatible semiconductor quantum dots: from biosynthesis and bioconjugation to biomedical application. *Chem Rev* 2015; **115**: 11669–11717.
9 Bain LE, Ivanisevic A. Engineering the cell-semiconductor interface: a materials modification approach using II-VI and III-V semiconductor materials. *Small* 2015; **11**: 768–780.
10 Silvi S, Credi A. Luminescent sensors based on quantum dot–molecule conjugates. *Chem Soc Rev* 2015; **44**: 4275–4289.
11 Wu P, Yan XP. Doped quantum dots for chemo/biosensing and bioimaging. *Chem Soc Rev* 2013; **42**: 5489–5521.
12 Zhou B, Shi BY, Jin DY, Liu XG. Controlling upconversion nanocrystals for emerging applications. *Nat Nanotechnol* 2015; **10**: 924–936.
13 Liu JN, Bu WB, Shi JL. Silica coated upconversion nanoparticles: A versatile platform for the development of efficient theranostics. *Acc Chem Res* 2015; **48**: 1797–1805.
14 Han SY, Deng RR, Xie XJ, Liu XG. Enhancing luminescence in lanthanide-doped upconversion nanoparticles. *Angew Chem Int Ed* 2014; **53**: 11702–11715.
15 Chen GY, Qiu HL, Prasad PN, Chen XY. Upconversion nanoparticles: design, nanochemistry, and applications in theranostics. *Chem Rev* 2014; **114**: 5161–5214.
16 Wu S, Butt HJ. Near-infrared-sensitive materials based on upconverting nanoparticles. *Adv Mater* 2016; **28**: 1208–1226.
17 Zhou W, Gao X, Liu DB, Chen XY. Gold nanoparticles for in vitro diagnostics. *Chem Rev* 2015; **115**: 10575–10636.
18 Saha K, Agasti SS, Kim C, Li XN, Rotello VM. Gold nanoparticles in chemical and biological sensing. *Chem Rev* 2012; **112**: 2739–2779.
19 Yue GZ, Su S, Li N, Shuai MB, Lai XC *et al*. Gold nanoparticles as sensors in the colorimetric and fluorescence detection of chemical warfare agents. *Coord Chem Rev* 2016; **311**: 75–84.
20 Dykman L, Khlebtsov N. Gold nanoparticles in biomedical applications: recent advances and perspectives. *Chem Soc Rev* 2012; **41**: 2256–2282.
21 Giljohann DA, Seferos DS, Daniel WL, Massich MD, Patel PC *et al*. Gold nanoparticles for biology and medicine. *Angew Chem Int Ed* 2010; **49**: 3280–3294.
22 Yau SH, Varnavski O, Goodson T. III. An ultrafast look at Au nanoclusters. *Acc Chem Res* 2013; **46**: 1506–1516.
23 Palmal S, Jana NR. Gold nanoclusters with enhanced tunable fluorescence as bioimaging probes. *Wiley Interdiscip Rev Nanomed Nanobiotechnol* 2014; **6**: 102–110.
24 Lu YZ, Chen W. Sub-nanometre sized metal clusters: from synthetic challenges to the unique property discoveries. *Chem Soc Rev* 2012; **41**: 3594–3623.
25 Shang L, Dong SJ, Nienhaus GU. Ultra-small fluorescent metal nanoclusters: synthesis and biological applications. *Nano Today* 2011; **6**: 401–418.
26 Tao Y, Li MQ, Ren JS, Qu XG. Metal nanoclusters: novel probes for diagnostic and therapeutic applications. *Chem Soc Rev* 2015; **44**: 8636–8663.
27 Yuan X, Dou XY, Zheng KY, Xie JP. Recent advances in the synthesis and applications of ultrasmall bimetallic nanoclusters. *Part Part Syst Charact* 2015; **32**: 613–629.
28 Chen LY, Wang CW, Yuan ZQ, Chang HT. Fluorescent gold nanoclusters: recent advances in sensing and imaging. *Anal Chem* 2015; **87**: 216–229.
29 Botchway SW, Charnley M, Haycock JW, Parker AW, Rochester DL *et al*. Time-resolved and two-photon emission imaging microscopy of live cells with inert platinum complexes. *Proc Natl Acad Sci USA* 2008; **105**: 16071–16076.
30 Shi HF, Sun HB, Yang HR, Liu SJ, Jenkins G *et al*. Cationic polyfluorenes with phosphorescent iridium(III) complexes for time-resolved luminescent biosensing and fluorescence lifetime imaging. *Adv Funct Mater* 2013; **23**: 3268–3276.
31 Shang L, Azadfar N, Stockmar F, Send W, Trouillet V *et al*. One-pot synthesis of near-infrared fluorescent gold clusters for cellular fluorescence lifetime imaging. *Small* 2011; **7**: 2614–2694.
32 Howard SS, Straub A, Horton NG, Kobat D, Xu C. Frequency-multiplexed in vivo multiphoton phosphorescence lifetime microscopy. *Nat Photonics* 2013; **7**: 33–37.

33 Holwerda KM, Karumanchi SA, Lely AT. Hydrogen sulfide: role in vascular physiology and pathology. *Curr Opin Nephrol Hypertens* 2015; **24**: 170–176.

34 Li L, Rose P, Moore PK. Hydrogen sulfide and cell signaling. *Annu Rev Pharmacol Toxicol* 2011; **51**: 169–187.

35 Szabo C. Roles of hydrogen sulfide in the pathogenesis of diabetes mellitus and its complications. *Antioxid Redox Signaling* 2012; **17**: 68–80.

36 Lan AP, Xu WM, Zhang H, Hua XX, Zheng DD *et al.* Inhibition of ROS-activated p38MAPK pathway is involved in the protective effect of H2S against chemical hypoxia-induced inflammation in PC12 cells. *Neurochem Res* 2013; **38**: 1454–1466.

37 Kulkarni KH, Monjok EM, Zeyssig R, Kouamou G, Bongmba ON *et al.* Effect of hydrogen sulfide on sympathetic neurotransmission and catecholamine levels in isolated porcine iris-ciliary body. *Neurochem Res* 2009; **34**: 400–406.

38 Zhang KY, Zhang J, Liu YH, Liu SJ, Zhang PL *et al.* Core–shell structured phosphorescent nanoparticles for detection of exogenous and endogenous hypochlorite in live cells via ratiometric imaging and photoluminescence lifetime imaging microscopy. *Chem Sci* 2015; **6**: 301–307.

39 Chen ZJ, Zhang KY, Tong X, Liu YH, Hu CY *et al.* Phosphorescent polymeric thermometers for in vitro and in vivo temperature sensing with minimized background interference. *Adv Funct Mater* 2016; **26**: 4386–4396.

40 Zhao Q, Zhang C, Liu S, Liu Y, Zhang KY *et al.* Dual-emissive polymer dots for rapid detection of fluoride in pure water and biological systems with improved reliability and accuracy. *Sci Rep* 2015; **5**: 16420.

41 Hutchinson CL, Lakowicz JR, Sevick-Muraca EM. Fluorescence lifetime-based sensing in tissues: a computational study. *Biophys J* 1995; **68**: 1574–1582.

42 Berezin MY, Achilefu S. Fluorescence lifetime measurements and biological imaging. *Chem Rev* 2010; **110**: 2641–2684.

43 Yu Q, Zhang KY, Liang H, Zhao Q, Yang TS *et al.* Dual-emissive nanohybrid for ratiometric luminescence and lifetime imaging of intracellular hydrogen sulfide. *ACS Appl Mater Interfaces* 2015; **7**: 5462–5470.

44 Shi H, Ma X, Zhao Q, Liu B, Ou Q *et al.* Ultrasmall phosphorescent polymer dots for ratiometric oxygen sensing and photodynamic cancer therapy. *Adv Funct Mater* 2014; **24**: 4823–4830.

45 Sun J, Yue Y, Wang P, He HL, Jin YD. Facile and rapid synthesis of water-soluble fluorescent gold nanoclusters for sensitive and selective detection of Ag+. *J Mater Chem C* 2013; **1**: 908–913.

46 Zhou C, Sun C, Yu MX, Qin YP, Wang JG *et al.* Luminescent gold nanoparticles with mixed valence states generated from dissociation of polymeric Au(I) thiolates. *J Phys Chem C* 2010; **114**: 7727–7732.

47 Zhou R, Shi M, Chen X, Wang M, Chen H. Atomically monodispersed and fluorescent sub-nanometer gold clusters created by biomolecule-assisted etching of nanometer-sized gold particles and rods. *Chem Eur J* 2009; **15**: 4944–4951.

48 Liu CL, Ho ML, Chen YC, Hsieh CC, Lin YC *et al.* Thiol-functionalized gold nanodots: two-photon absorption property and imaging in vitro. *J Phys Chem C* 2009; **113**: 21082–21089.

49 Huang CC, Yang ZS, Lee KH, Chang HT. Synthesis of highly fluorescent gold nanoparticles for sensing mercury (II). *Angew Chem Int Ed* 2007; **46**: 6824–6828.

50 Chang HY, Chang HT, Hung YL, Hsiung TM, Lin YW *et al.* Ligand effect on the luminescence of gold nanodots and its application for detection of total mercury ions in biological samples. *RSC Adv* 2013; **3**: 4588–4597.

51 Sun J, Yang F, Zhao D, Chen CX, Yang XR. Integrated logic gate for fluorescence turn-on detection of histidine and cysteine based on Ag/Au bimetallic nanoclusters–Cu2+ ensemble. *ACS Appl Mater Interfaces* 2015; **7**: 6860–6866.

52 Goswami N, Lin FX, Liu YB, Leong DT, Xie JP. Highly luminescent thiolated gold nanoclusters impregnated in nanogel. *Chem Mater* 2016; **28**: 4009–4016.

53 Kremers GJ, Goedhart J, van Munster EB, Gadella TWJ Jr. Cyan and yellow super fluorescent proteins with improved brightness, protein folding, and FRET Förster radius. *Biochemistry* 2006; **45**: 6570–6580.

54 Papapetropoulos A, Pyriochou A, Altaany Z, Yang G, Marazioti A *et al.* Hydrogen sulfide is an endogenous stimulator of angiogenesis. *Proc Natl Acad Sci USA* 2009; **106**: 21972–21977.

55 Ren MG, Deng BB, Kong XQ, Zhou K, Liu KY *et al.* A TICT-based fluorescent probe for rapid and specific detection of hydrogen sulfide and its bio-imaging applications. *Chem Commun* 2016; **52**: 6415–6418.

56 Liu J, Guo XD, Hu R, Liu XY, Wang SQ *et al.* Molecular engineering of aqueous soluble triarylboron-compound-based two-photon fluorescent probe for mitochondria H2S with analyte-induced finite aggregation and excellent membrane permeability. *Anal Chem* 2016; **88**: 1052–1057.

57 Zhao CC, Zhang XL, Li KB, Zhu SJ, Guo ZQ *et al.* Förster resonance energy transfer switchable self-assembled micellar nanoprobe: ratiometric fluorescent trapping of endogenous H2S generation via fluvastatin-stimulated upregulation. *J Am Chem Soc* 2015; **137**: 8490–8498.

58 Lutolf MP, Tirelli N, Cerritelli S, Cavalli L, Hubbell JA. Systematic modulation of Michael-type reactivity of thiols through the use of charged amino acids. *Bioconjugate Chem* 2001; **12**: 1051–1056.

59 Liu QL, Du HZ, Ren XZ, Bian WZ, Fan L *et al.* Design of ratiometric emission probe with visible light excitation for determination of Ca2+ in living cells. *Anal Chem* 2014; **86**: 8025–8030.

60 Devireddy LR, Hart DO, Goetz DH, Green MR. A mammalian siderophore synthesized by an enzyme with a bacterial homolog involved in enterobactin production. *Cell* 2010; **141**: 1006–1017.

61 Gaussin V, Gailly P, Gills J-M, Hue L. Fructose-induced increase in intracellular free Mg2+ ion concentration in rat hepatocytes: relation with the enzymes of glycogen metabolism. *Biochem J* 1997; **326**: 823–827.

62 Frederickson CJ, Koh J-Y, Bush AI. The neurobiology of zinc in health and disease. *Nat Rev Neurosci* 2005; **6**: 499–462.

63 Liu J, Karpus J, Wegner SV, Chen PR, He C. Genetically encoded copper(I) reporters with improved response for use in imaging. *J Am Chem Soc* 2013; **135**: 3144–3149.

64 Mosmann T. Rapid colorimetric assay for cellular growth and survival: Application to proliferation and cytotoxicity assays. *J Immunol Meth* 1983; **65**: 55–63.

65 Wang X, Sun J, Zhang WH, Ma XX, Lv LZ *et al.* A near-infrared ratiometric fluorescent probe for rapid and highly sensitive imaging of endogenous hydrogen sulfide in living cells. *Chem Sci* 2013; **4**: 2551–2556.

66 Zhao WM, Zhang J, Lu YJ, Wang R. The vasorelaxant effect of H2S as a novel endogenous gaseous KATP channel opener. *EMBO J* 2001; **20**: 6008–6016.

67 Kumai Y, Porteus CS, Kwong RWM, Perry SF. Hydrogen sulfide inhibits Na+ uptake in larval zebrafish, Danio rerio. *Pflugers Arch* 2015; **467**: 651–664.

Supplementary Information for this article can be found on the *Light: Science & Applications*' website (http://www.nature.com/lsa).